Journal of the European Ceramic Society **19** (1999) 2191–2209

PII: S0955-2219(99)00102-8
0955-2219/99/$ - see front matter

Surface and Interface Properties of Alumina via Model Studies of Microdesigned Interfaces

M. Kitayama ,[ab†] J. D. Powers, [ab‡] L. Kulinsky [ab] and A. M. Glaeser [ab*]

[a]Department of Materials Science and Mineral Engineering, 787 Evans Hall, MC 1760, University of California, Berkeley, CA 94720-1760, USA
[b]Center for Advanced Materials, Lawrence Berkeley National Laboratory, Berkeley, CA 94720, USA

Abstract

The ability to produce controlled-geometry, controlled-crystallography internal voids in ceramics has made possible several new model experiments for studying the high-temperature properties of surfaces and interfaces in ceramics. Recent advances have enabled the production of more complex microdesigned internal defect structures, and have exploited new means of examining them, thus, broadening the range of problems that can be addressed. A particular topic of concern is the effect of surface energy anisotropy on both the driving force for and the mechanism of shape changes. This paper reviews and previews recent research focussing on improving our understanding of surface diffusion in ceramics. Rayleigh instabilities provide one means of examining morphological evolution. The modelling of Rayleigh instabilities in materials with surface energy anisotropy is reviewed, and the results of experiments utilizing microdesigned pore arrays in sapphire are summarized. In a material with anisotropic surface energy and a facetted Wulff shape, the driving force for shape changes hinges on both the absolute and relative surface energies. Microdesigned pore structures have been used to determine the stable surfaces in both undoped and doped sapphire and to provide the relative values of the energies of these stable surfaces. Nonequilibrium shape, controlled-crystallography cavities have been introduced into undoped sapphire, and the effect of crystallographic orientation on their morphological evolution has been studied. Comparisons of the results with predictions of models of surface-diffusion-controlled evolution indicate that surface-attachment-limited kinetics (SALK) play an important role. © *1999 Elsevier Science Ltd. All rights reserved.*

Keywords: surface diffusion, surface energy, interfaces, porosity, Al_2O_3.

1 Introduction

To achieve optimum properties in ceramics, it is necessary to control the evolution of the microstructure, and highly desirable that this control is based on fundamental understanding of the evolution process. A complete understanding of microstructural evolution requires that the many interacting and competing processes that collectively dictate the spatial and temporal characteristics of microstructural change be understood. The barriers to such an understanding are significant.

The geometric details of a powder compact—the particle size, particle distribution, packing density, packing density variations—play a major role in determining the driving forces for mass transport and microstructural change. In systems in which the surface and interfacial properties are isotropic and known, knowledge of the geometry, i.e. the local curvatures, can be sufficient to describe these driving forces. In real systems, the surface energy is anisotropic and grain boundary properties can depend on both misorientation and boundary plane orientation. For such systems, a description of the driving force is much more complex, and the variations of driving force within the compact are likely to be larger than in idealized isotropic materials.

The driving forces for mass transport can be dissipated by several transport mechanisms that operate largely in parallel: surface diffusion, evaporation-condensation, lattice diffusion and grain

*To whom correspondance should be addressed. Fax: +1-510-486-6086; e-mail: aglaeser@sapphire.berkeley.edu
†Now at Synergy Ceramics Laboratory, Fine Ceramics Research Association, 1-1 Hirate-cho, Kita-ku, Nagoya 462 Japan.
‡Now at Allied Signal Inc., Box 1021, 101 Columbia Road, Morristown, NJ 07962-1021, USA.

boundary diffusion. In the simplest situations, mass flows occurs *predominantly* along a single path, e.g. through the vapor phase, through the bulk, along a solid–vapor interface (a surface) or along a solid–solid interface (a grain boundary). The *rate* of microstructural change can be limited by the rate of mass arrival via gas, bulk, surface, or grain boundary diffusion. Alternatively, the rate of shape change can be limited by the rate at which mass can be incorporated at a mass sink or can be released or supplied by a mass source. In this situation, the rate of a nucleation step or of an attachment/detachment step limits the shape change rate. The general term surface-attachment-limited kinetics (SALK) is used to describe these cases.

More often, more than one mass transport mechanism may be important. The *nature* of the microstructure produced depends upon the relative rates of the competing transport mechanisms. Surface diffusion and evaporation–condensation can contribute to particle coarsening and interparticle neck growth without densification, while lattice diffusion and grain boundary diffusion lead to neck growth, but also produce particle-particle approach. The processing conditions used must be consistent with the microstructural objectives. The importance of controlling the densification: coarsening ratio is recognized, and has been the subject of considerable theoretical and experimental effort (e.g. Refs 1–4).

As an aid to designing and processing materials with useful microstructures and properties, and maintaining these microstructures and properties during subsequent use at elevated temperature, it would be clearly be advantageous to have reliable and robust models of microstructural evolution, and a complete and reliable database of the materials properties (thermodynamic and kinetic) that are required input for these models. The thermodynamic *and* kinetic properties of surfaces and interfaces will be key components of this database.

The successful modelling of microstructural development and microstructural stability is clearly difficult. Choices must be made regarding the extent to which anisotropy of surface and interfacial properties will be incorporated. This will affect the driving force description, and may also fundamentally alter the path of evolution. From a practical perspective, it also affects the complexity of the model. In order to determine the potential contributions of competing transport mechanisms, reliable values for the transport coefficients and interfacial reaction rate constants are required. To simplify modelling, or because the necessarily information is unavailable, or both, simple geometries, isotropic surface and interfacial properties, and a single dominant transport process are often assumed (e.g. Refs 5–8). Real systems are generally more complex. The materials are anisotropic, the geometries differ from those that are assumed, multiple processes interact and compete, and the relative importance of the competing processes can change as the microstructure changes at elevated temperature.

Models treating a variety of diVusion-limited shape changes in idealized single-phase materials with isotropic surface energies were developed during the 1950s and 1960s. These included treatments of surface (scratch) smoothing,[9] grain boundary grooving,[10] particle sintering,[4–7] and Rayleigh instabilities of solid rods and cylindrical cavities in solids.[8] These models served two important roles. In cases where the relevant transport data was available, the models could be used in a predictive manner. In cases where transport data was absent, the experimental results could be evaluated using these models to provide needed transport data. A significant fraction of the surface diffusion data available for ceramic systems has been inferred from rates of morphological change assumed to be controlled by surface diffusion.

Subsequent treatments of the aforementioned processes have focussed on extending their range of applicability, and examining the behavior of less idealized systems. Accordingly, some efforts have focussed on evaluating the effects of higher-order (nonlinear) terms on the predictions of the model and improving the accuracy of predictions for more advanced stages of these processes (e.g. Refs 11 and 12). Others have focussed on the effects of more complex initial or other boundary conditions on the predicted behavior.[13,14] In general, these analyses have retained the isotropic surface energy assumption characteristic of the original models.

Other modelling refinements have focussed on incorporating the effects of surface energy anisotropy on morphological evolution. For a particle or cavity of fixed volume held at constant temperature, the driving force for shape changes is the associated reduction in the total surface energy. The equilibrium shape of a crystal or cavity is that which minimizes its total surface energy. In many crystalline solids, the lowest energy form of a particle or cavity includes facets, and the equilibrium or Wulff shape can be fully facetted. The Wulff theorem prescribes that the equilibrium shape of a facetted N-sided polyhedral particle or cavity is that for which

$$\frac{\gamma_1}{l_1} = \frac{\gamma_2}{l_2} = \frac{\gamma_3}{l_3} = \ldots = \frac{\gamma_i}{l_i} = \text{constant} \qquad (1)$$

where γ_i is the energy per unit area of the ith facet, and l_i denotes the physical distance from the center

of mass of the crystal to the ith facet measured along a normal to the *i*th facet.[15] Surface energy anisotropy will thus alter the final state that a system tends to, and will influence the driving forces and kinetics of the processes that transform the system from an initial nonequilibrium state to the equilibrium state.[16] The appearance of facets can also lead to a change in the rate-controlling mechanism.

The influence of surface energy anisotropy and facetting on the energetics and kinetics of shape changes has become the topic of increasing attention. Bonzel, Mullins and their collaborators have examined the effect of surface energy anisotropy on scratch smoothing behavior, and have developed elegant new experimental methods and refined theoretical models.[17–22] Cahn, Taylor, Carter, and colleagues[23–25] have addressed a broad range of problems involving shape changes in facetted crystals, and have provided theoretical descriptions of shape changes controlled by both surface diffusion and by SALK.

The experimentalist also faces difficult decisions when investigating a particular aspect of microstructural evolution. Conventional experiments using ceramic powder compacts and polycrystals have the advantage that they use a 'real' powder or a 'real' material. However, the disadvantage is that such powders and materials generally provide a very limited ability to control the relevant microstructural and crystallographic parameters that are important. As a result, particularly as more complex (and hopefully more accurate) models are developed, experiments on compacts and polycrystals may not provide the most convenient route to testing and validating these models. A general goal of our work has been to develop an experimental method that provides control over the pore, flaw, or second phase geometry, that allows the crystallography and chemistry of surfaces and interfaces to be controlled, and that in some cases, provides the ability to alter the relative contributions of coarsening and densification processes. It was our hope that such a method would help further our fundamental understanding of both the thermodynamics and kinetics of microstructural evolution.

Within the past decade, several new model experiments were developed for examining the high-temperature properties of surfaces and interfaces in ceramics. These experiments exploit standard microlithographic techniques indigenous to semiconductor processing to produce defects and microstructures that closely simulate those that have been theoretically modelled. These techniques have been adapted to allow the introduction of large numbers of cavities of controlled size, shape, and spacing into ceramic surfaces of known crystallographic orientation and controlled purity.[26,27] Internal cavities are produced by solid-state diffusion bonding a substrate with surface cavities to a second cavity-free substrate in a vacuum hot press. The resulting internal 'microdesigned' defect arrays have formed the basis of experiments examining a wide range of phenomena, including high-temperature crack healing,[28–30] Rayleigh instabilities,[28–31] pore-boundary interactions,[32] grain boundary migration,[33,34] and pore coarsening and pore elimination.[35] More recent work has focussed on the development and application of new model experiments that would help to quantify the anisotropy of surface and interfacial properties, and reveal more clearly the effect of this anisotropy on microstructural evolution.

Computational and modelling capabilities already surpass experimental capabilities in several areas. The size and complexity of simulations is expanding rapidly, and the gap between the spatial and temporal scale of what is modelled and what is of interest to the practicing ceramist is decreasing. There is an increasing need for model experiments that can test and validate existing and emerging models of microstructural evolution. This is particularly so for computational approaches that predict fundamental properties of materials such as surface energies and segregation behavior (e.g. Refs 36–40). Without such confirmation the incentive for additional efforts in this direction is reduced, and the predictions that have been made may be met with undue skepticism. Accordingly, his paper has two primary objectives. These are: (1) to describe the technique and its capabilities, and (2) to summarize some recent advances and developments that form the basis for on-going research. It is hoped that this presentation will encourage the more widespread use of the techniques that have been developed, and the design and application of new model experiments. It is our hope that such experiments will be exploited by the community to test existing models of microstructural evolution, and help guide the development of more accurate and useful models where current models are shown to be inadequate.

2 Fabrication of Microdesigned Interfaces

Lithography facilitates the study of a wide range of processes that occur during material fabrication or during subsequent use at high temperature. The combination of photolithographic methods, ion beam etching, and hot pressing provides the ability to define and introduce surface features (cavities) with a controlled geometry and location, and to

subsequently transform these surface features into internal features. A brief summary of the procedure and references to prior studies follows. A more detailed description of the experimental methods can be found in Refs 26 and 27.

The basic processing steps in the production of a sample with a microdesigned interface are (1) resist coating, (2) exposure, (3) etching, (4) sample assembly, and (5) bonding, as illustrated in Fig. 1. The first four steps are normally performed in Class 100 clean room conditions, thus minimizing the potential for inadvertent contamination of the surfaces of interest.

The substrate, normally a single crystal wafer or a dense polycrystal, is coated with a uniformly thick photoresist layer. Although the vast majority of our research has used either sapphire single crystals or theoretically dense, high-purity undoped or doped alumina as the substrate, experiments have also been performed in which glass-bonded alumina, lithium fluoride, silicon, fused silica, lead borosilicate glass, and soda-lime silica glass were used. Current efforts are focussing on application of the method to silicon carbide and silicon nitride. Using a typical range of processing conditions, the thickness of the photoresist can be varied from 1·3 to 2·6 μm. The photoresist is then selectively exposed using UV radiation.

The shape of the exposed features reflects the mask pattern. The geometry of features on the mask is defined using pattern generation software. Figure 2 shows schematic examples of the types of patterns that can be generated on a mask. Lines and other features that can be assembled from square design elements are particularly easy to produce; features with smoothly curved edges must be built up using these square elements and are as a result more tedious to assemble. For positive photoresists, exposure increases the solubility of the photoresist and allows its selective removal, thus exposing the substrate. Negative photoresists are also available, and here the *unexposed regions* are preferentially removed. A mask that produces isolated defects with a positive resist produces a continuous pore phase when used with a negative resist. An ion beam is used to etch the exposed ceramic surface, and thereby transfer the mask pattern to the ceramic substrate. Etching of the substrate and residual resist occurs simultaneously. Thus, unless thicker resists are used, or other barriers to etching are deposited on the surface, the practically accessible feature depth is limited to a maximum of a few tenths of a micron.

Conventional lithographic procedures allow the fabrication of features with minimum (lateral) dimensions of order one to two microns; these features can be repeated up to $\approx 10^6$ times on a single substrate. Under optimum conditions, the location of the features can be controlled to within $\approx \pm 0{\cdot}1$ μm. With a typical feature depth of a few tenths of a micron, the minimum accessible feature volume is < 1 μm^3. Even smaller features can be produced using so-called nanofabrication facilities. With e-beam lithography, the relevant size scale of features decreases by roughly one order of magnitude, i.e. features with widths of the order of 0·1–0·2 μm can be produced. This broadens the size scale of accessible features, and allows greater control and flexibility when complex shapes involved curves are required. The specific experimental objectives dictate the

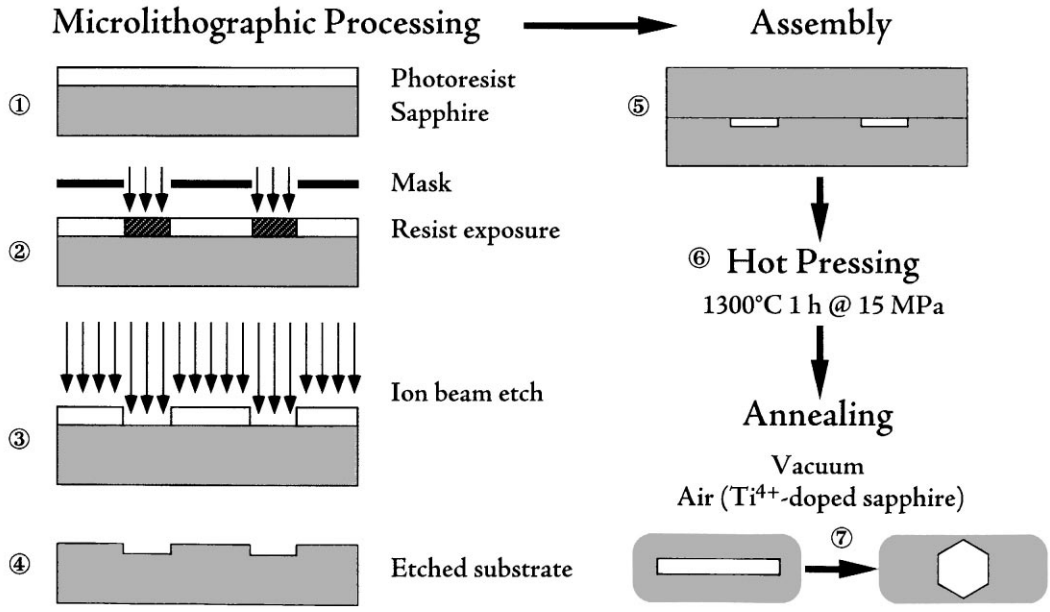

Fig. 1. Illustration of processing steps in production of microdesigned interfaces. A broad range of interfacial microstructures can be produced. The noneequilibrium nature of the defect shape after bonding allows studies of crack healing and of the rate at which the Wulff shape is reached.

design of the surface structures, and the methods required to fabricate them.[26,27,35]

After etching and just before diffusion bonding, an unetched and an etched substrate are placed in contact (again under clean room conditions). For sapphire and alumina, the surface features are converted to internal features by vacuum hot pressing (1300°C, 1 h, 15 MPa bonding pressure, $2{\cdot}6 \times 10^{-3}$ Pa vacuum). By changing the materials that are assembled, and the details of the assembly process, a wide variety of ensembles addressing a broad range of experimental objectives can be produced. Specimens prepared by bonding an etched single crystal to an unetched single crystal of identical orientation provide a means of simulating defects in single crystals, i.e. intragranular flaws. When the substrates are aligned so that crystallographic directions in the surface plane are 'parallel', in reality a low-angle twist boundary is produced. However, with care, twist angles of $< 1°$ can be achieved, and one approaches an intergranular defect. By increasing the twist angle, a high-angle grain boundary, and controlled-misorientation bicrystals can be prepared to study intergranular defects. Single crystal-polycrystal ensembles and polycrystal-polycrystal ensembles provide an opportunity to examine the effects of a wider range of misorientation, and to simulate and study defects in typical polycrystalline materials. Doped polycrystalline samples can be made by conventional routes to examine impurity effects. Crack healing studies by Powers *et al.*[29,30] have demonstrated that ion implantation can also be a useful method of introducing controlled levels of impurities in the near-surface layer, and assessing their effect on feature evolution. Using glass substrates, internal voids/bubbles of controlled size, shape and spacing can be generated. In principle, the features can also be filled with a suitable metal or second phase to allow the generation of model 'composite' interfaces. Dissimilar materials can also be bonded, allowing, for example, the introduction of highly controlled (potentially strength-limiting) defects at ceramic–metal interfaces. In virtually all experiments, it is necessary to minimize the morphological changes of the defect structure during bonding so that the evolution of the 'as-bonded' structure can be examined during subsequent annealing.

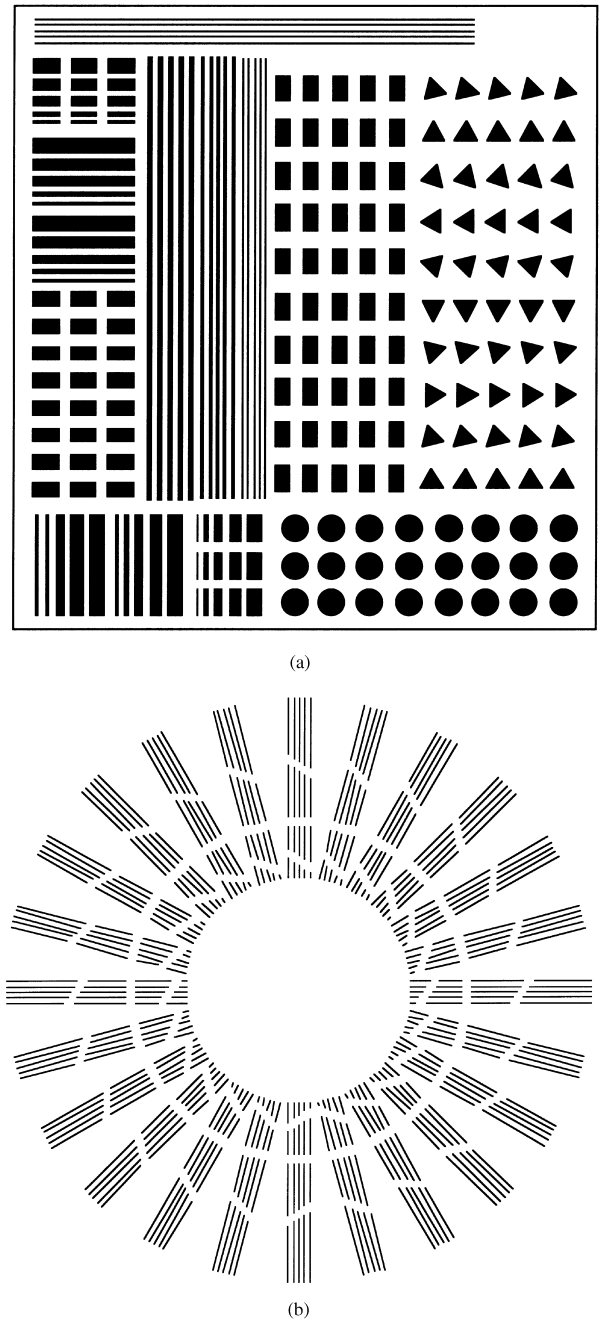

Fig. 2. Schematic illustration of mask patterns used to generate microdesigned internal defect patterns: (a) pattern consisting of rectangular, circular, and triangular features of varying size, shape, and orientation as well as high aspect ratio channels. The former were used to investigate crack healing, the latter to investigate Rayleigh instabilities; (b) pattern of controlled and varied aspect ratio channels with channel orientation (the orientation dependence of surface energy anisotropy) on Rayleigh instabilities.

For some applications, such as the fabrication of calibration standards for nondestructive evaluation methods, the sole objective is to control the geometry of the defect structure and to characterize the 'as-bonded' defects using a variety of techniques. Thus, using lithography, internal cracklike defects of controlled size, shape, and spacing can be generated in optically transparent materials such as sapphire or glass. Optical microscopy can be used to confirm the defect pattern. Acoustic microscopy can then be performed on these standards to quantify the resolution limit of the NDE method.[41] Optically transparent materials that have acoustic properties like those of opaque materials can also be prepared; crystals and glasses that mimic the acoustic response of Ni-based alloys, Ti-based alloys, and Si-based ceramics have been identified, and standards for acoustic microscopy have been fabricated.

In the vast majority of the work, it is the evolution of the internal features during high-temperature annealing that is of primary interest. For sapphire and other optically transparent materials, optical microscopy provides a convenient nondestructive method of observation for all but the finest scale features. Using this method, a single sample can be annealed, and the morphological changes can then be characterized. This sequence can be repeated to allow study of the time evolution of specific defects. When greater resolution is required, or when an opaque material is used, fracture surfaces can be examined by optical or scanning electron microscopy. For the finest features, or when even higher spatial resolution is required, foils containing interfacial structures can be prepared, and examined using transmission or scanning transmission electron microscopy. Here one of the difficulties may become distinguishing the defects that are introduced from those that arise from polishing scratches and other irregularities in the substrate surfaces. More recently, atomic force microscopy has been used as a tool for more detailed study of the surface topography,[42,43] and in principle, could also be used with suitable materials to examine the more nearly atomic level structure of surfaces undergoing morphological change.

In summary, the general fabrication method is applicable to a broad range of materials and material combinations. The available mask design tools make it possible to produce a wide variety of defect structures. As a result, model experiments addressing a broad spectrum of materials science problems can be devised and implemented.

3 Model Studies of Surfaces and Interfaces

3.1 Crack healing and Rayleigh instabilities

The rate of morphological change in ceramics is influenced by both the driving force for and the mechanism of mass transfer, i.e. whether the rate of mass transport is limited by diffusion, or by SALK. A considerable fraction of our prior research utilizing microdesigned interfaces has focussed on morphological changes under conditions where surface diffusion plays an important and often dominant role. Characterization of surface diffusion is extremely difficult, and significant variations in reported values of surface diffusivities arise even in well-studied systems such as sapphire.[44–58] Impurities and crystallographically dependent values of the surface energy anisotropy are believed to be two key contributors to this variability.

The similarities between the morphological changes that occur during sintering and during high temperature crack healing, and the possibility that similar transport mechanisms control or affect these two processes, were recognized by Yen and Coble[50] and by Gupta.[54] These similarities have made crack healing studies a potential vehicle for improving our understanding of sintering, and of assessing the effects of impurities on surface properties and transport processes during sintering. In particular, crack healing studies provide a convenient means of assessing surface energy anisotropy effects.

The influence of surface orientation and surface energy anisotropy on crack healing behavior in sapphire became apparent in the initial studies on undoped sapphire.[28] Thousands of microdesigned cracklike flaws of identical geometry were 'embedded' in sapphire crystals of varying surface orientation using the procedures outlined previously. The difference in crack crystallography resulted in obvious differences in the morphological characteristics of crack healing during subsequent high-temperature annealing. The effect of impurities became evident when cracklike cavities of identical size and shape were embedded in sapphire single crystals of identical surface orientation whose surfaces had been implanted with low levels (<300 ppma maximum, 100 ppma mean concentration in region of interest) of impurities commonly found in, or commonly added to aluminum oxide.[29,30] Rectangular cracks, ($\approx 100 \times 200$ μm; etch depth $\approx 0{\cdot}16$ μm) were introduced into *c*-axis (0001 surface) sapphire implanted with Ca, Mg, and Ti. To assure consistency of not only the crack face orientation, but also the crack *edge* crystallography, the crack edges were consistently oriented parallel to the $[11\bar{2}0]$ and $[1\bar{1}00]$ directions. During subsequent annealing at 1700°C, significant differences in the morphological evolution were evident, as illustrated in Fig. 3. While undoped and Mg-doped sapphire were qualitatively similar, the introduction of Ca led to rapid healing and the addition of Ti appeared to particularly stabilize features oriented parallel to the $[1\bar{1}00]$ direction.

The combined use of microfabrication techniques, ion implantation, and diffusion bonding thus provides a convenient means of studying the effects of specific impurities on crack healing behavior. Crack healing studies in Mg-, Ca- and Ti-implanted sapphire indicated that each impurity affects the morphological evolution of defects, and does so in a distinct manner. While Mg additions appear to have a slight accelerating effect on the rate of healing, the effects of Ca and Ti additions are more dramatic. The distinctions would be difficult to identify from the results of more conventional experiments, e.g. sintering studies. One rationalization of the results would be to ascribe the

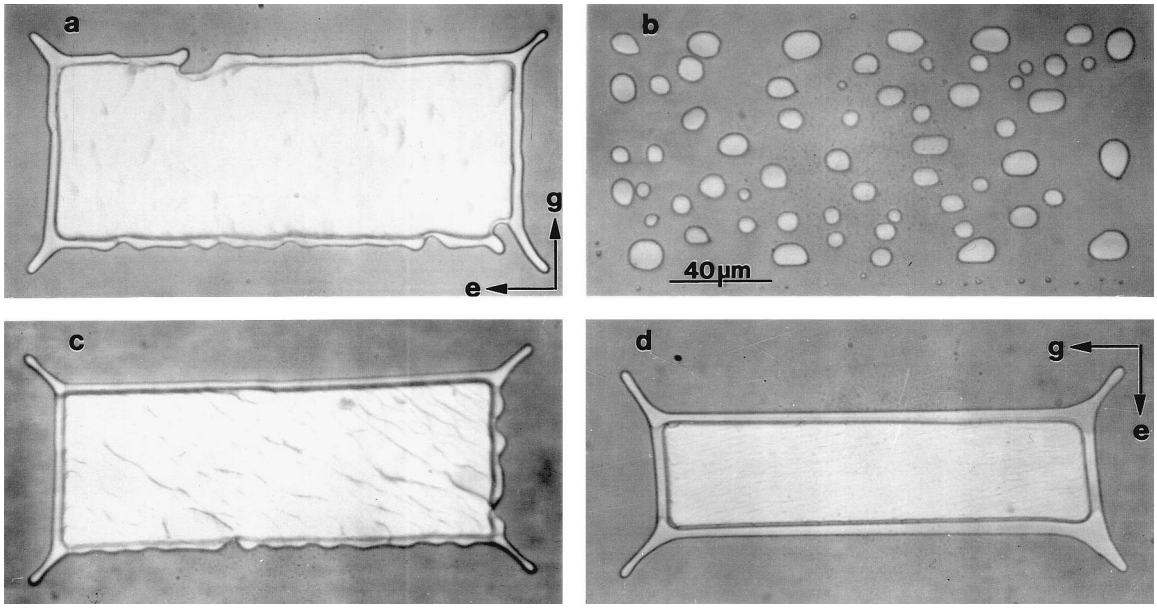

Fig. 3. Cracks in (a) undoped, (b) Ca-implanted, (c) Mg-implanted, and (d) Ti-implanted sapphire, after annealing times of 140 min (b,c) and 200 min (a, d). Note especially the drastic difference in healing behavior brought about by Ca additions, and the increased stability of crack edges brought about by Ti additions. The crack edge directions are: e = [11$\bar{2}$0], g = [1$\bar{1}$00]. Orientations in (a, b, c) are as indicated in a; the orientations in (d) are reversed as indicated

significant difference in evolution rates to a change in the magnitude of the surface diffusivity. The observation of distinct morphologies led us to suspect that impurity-segregation induced changes in the surface energy anisotropy and possibly the nature of the stable surfaces might be responsible.

Our interest in understanding how these dopants assist or impede sintering, and impact other aspects of microstructural evolution and stability, prompted further model studies of crack healing, more specifically, examining the late stages of healing in which 'cylindrical' pore channels undergo Rayleigh instabilities.[29–31] In conjunction with these model studies, efforts were made to model this stage of crack healing, and to incorporate effects of surface energy anisotropy.[59,60] This body of work has recently been reviewed, and the interested reader is referred to Ref. 61 for a more detailed presentation. A brief summary of the key features follows.

Measurement and interpretation of the breakup characteristics of 'cylindrical' pore channels are major aspects of the work in Refs 29–31. The spatial and temporal characteristics of such Rayleigh instabilities have the potential to provide a wealth of information relating to the thermodynamic and kinetic properties of surfaces. Thermodynamic and kinetic information can be inferred from the values of the minimum wavelength for perturbation growth, λ_{min}, the wavelength of maximum (most rapid) instability, λ_{max}, and the time t required for breakup of a continuous channel into isolated particles or pores.

Analyses of the morphological instability of continuous phases, such as those presented by Plateau,[62] Rayleigh,[63] Nichols and Mullins,[64] and others subsequently, focus on the stability of a cylindrical body with isotropic surface free energy to sinusoidal perturbations of infinitesimal amplitude. Two key quantities emerge from such analyses. The first quantity imposes a thermodynamic limit on the process, while the second is relevant to the kinetics of evolution.

For materials with isotropic γ_s, the thermodynamic minimum or critical wavelength λ_{min} that must be exceeded if there is to be a driving force for the amplitude to increase is $2\pi R$ (the cylinder circumference).[62] In an isotropic system, infinitesimal perturbations with $\lambda < 2\pi R$ are predicted to decay. Only perturbations with $\lambda > \lambda_{min}$, i.e. $> 2\pi R$, increase in amplitude, and the magnitude of the interfacial area (and energy) reduction increases with increasing λ.

Nichols and Mullins extended the method of Plateau and Rayleigh to solids, and evaluated the mode of maximum instability for solid cylindrical rods,[64] and for the breakup of cylindrical voids in a solid via surface or lattice diffusion.[8] For a cylindrical void with isotropic surface energy, both the perturbation growth rate and the dominant wavelength depend upon the relative contributions of surface and lattice diffusion to breakup.[8] Surface diffusion dominated breakup is characterized by a wavelength of 8·89R ($=\sqrt{2}\cdot\lambda_{min}$); lattice diffusion dominated breakup has a characteristic wavelength of 13·2R ($\approx 2\cdot1\cdot\lambda_{min}$). The amplitude of the sinusoidal perturbation α increases (or decreases) exponentially with time t, at a rate that depends upon the magnitude of the so-called amplification factor μ, as described by eqn (2).

$$\alpha = \alpha_o \exp^{\mu t} \tag{2}$$

For surface-diffusion-controlled evolution,

$$\mu = \frac{D_s \gamma \nu \Omega^2}{\mathrm{R}^4 kT}\left[x^2\left(1-x^2\right)\right] = \frac{\delta_s D_s \gamma \Omega}{\mathrm{R}^4 kT}\left[x^2\left(1-x^2\right)\right] \tag{3}$$

where D_s is the surface self-diffusion coefficient, δ_s is the thickness of the zone in which surface diffusion occurs, γ_s the surface tension, ν the number of diffusing atoms per unit surface area, Ω the atomic volume, R the pore channel (or solid cylinder) radius, kT has its usual meaning, x represents the ratio $2\pi\mathrm{R}/\lambda$.

The subsequent analyses of Cahn,[65] Stölken and Glaeser,[59] and Glaeser[60] indicated that surface energy anisotropy would play a key role in altering the thermodynamic conditions and the kinetics of evolution. The analysis by Cahn showed that for a single crystal rod with a specific surface energy γ_s that is isotropic in the plane transverse to the cylinder axis (the R–θ plane), but a function of $\phi = (\partial \mathrm{R}/\partial z)$ where z is the axial coordinate,

$$\lambda_{\min} = 2\pi\mathrm{R}\left(1+\frac{1}{\gamma_s}\left(\frac{\partial^2\gamma_s}{\partial\phi^2}\right)\right)^{\frac{1}{2}} \tag{4}$$

The kinetically dominant wavelength is also shifted in comparison to its isotropic analogue. Stölken and Glaeser have shown that

$$\lambda_{\max} = \sqrt{2}\cdot 2\pi\mathrm{R}\left(1+\frac{1}{\gamma_s}\left(\frac{\partial^2\gamma_s}{\partial\phi^2}\right)\right)^{\frac{1}{2}} = \sqrt{2}\cdot\lambda_{\min} \tag{5}$$

It follows that when $(\partial^2\gamma_s/\partial\phi^2)$ is large and positive, as might be expected for a surface orientation corresponding to a sharp minimum in the γ_s plot, a substantial stabilization would be expected, and $\lambda_{\min} > 2\pi\mathrm{R}$, and $\lambda_{\max} > \sqrt{2}\cdot\lambda_{\min}$.

Table 1 summarizes the findings of experimental studies of pore channel instability in both undoped and implanted sapphire. High aspect ratio pore channels were introduced into the basal plane of sapphire single crystals using microlithographic processing methods, and oriented along the indicated directions. Samples were annealed at 1700°C, and the breakup characteristics of the pore channels were determined. Pore spacings were assumed to reflect $\lambda_{\max}$, and measured values were normalized by the radius R of a cylindrical channel with equal cross sectional area to allow a comparison with the predictions of an isotropic analysis. As is evident, *none* of the observations are compatible with an isotropic analysis. It is particularly noteworthy that although in undoped, Mg-doped and Ca-doped sapphire breakup was complete after several hours of annealing, the channels oriented parallel to $[1\bar{1}00]$ in Ti-doped sapphire survived hundreds of hours at 1700°C without undergoing breakup. Surface energy anisotropy can thus exert a very potent stabilizing influence.

Table 1. Spatial characteristics of Rayleigh instabilities in undoped[32] and ion-implanted[31,32] sapphire annealed at 1700°C

Sample	*Channel radius* R *(μm)*	*Mean* λ/R, *channels parallel to* $[1\bar{1}00]$	*Mean* λ/R *channels parallel to* $[11\bar{2}0]$
Isotropic	–	(8·89)	(8·89)
Undoped	0·33	45	130
Mg-doped	0·32	17	26
	0·32	–	63
Ca-doped	0·50	–	65
	0·71	–	62
Ti-doped	0·29	∞	78

Interpretations of the kinetic data from such studies (where effects of surface energy anisotropy are indicated) in terms of isotropic models can lead to significant errors.[60] For the simple anisotropic material considered, the modelling indicates that the amplification factor takes the form

$$\mu = \frac{\delta_s D_s \gamma_s \Omega}{\mathrm{R}^4 kT}\left[x^2\left(1-\left(1+\frac{1}{\gamma_s}\left(\frac{\partial^2\gamma_s}{\partial\phi^2}\right)\right)x^2\right)\right] \tag{6}$$

The magnitude and the sign of μ at a fixed value of λ (recall that $x = 2\pi\mathrm{R}/\lambda$) are impacted by the nature of the surface energy anisotropy. If an isotropic analysis is used to deduce a value for the surface diffusivity, an error will result that is described by

$$\frac{(D_s\delta_s)_{\text{apparent}}}{(D_s\delta_s)_{\text{actual}}} = \left[1+\frac{1}{\gamma_s}\left(\frac{\partial^2\gamma_s}{\partial\phi^2}\right)\right]^{-1} = \left[\frac{\lambda_{\max}^{\text{iso}}}{\lambda_{\max}^{\text{aniso}}}\right]^2 \tag{7}$$

Table 1 suggests that the wavelength ratio in eqn (7) can be smaller than 0·1, and thus, factor of >100 underestimates of the surface diffusivity are possible when surface energy anisotropy has a stabilizing effect. We note that while in Rayleigh instabilities the effects of anisotropy are relatively obvious, the effects in other experiments (e.g. scratch smoothing) may be equally important but much more difficult to detect.

Recent work examining Rayleigh instabilities has focussed on using mask design tools to allow the production of pore channels with a pre-existent perturbation of controlled amplitude and incrementally varied wavelength. The value of $\lambda_{\min}$ can then be determined by experimentally by establishing the smallest wavelength perturbation that increases in amplitude, and the value of $\lambda_{\max}$ can

be determined by identifying the wavelength that evolves most rapidly. Experiments were conducted on both undoped and Ti-doped sapphire, with the most complete set of results available for undoped sapphire. It was possible to estimate both λ_{min} and λ_{max} from the experimental data. Although the values of λ_{min} and λ_{max} varied with channel orientation (as expected), the modelling work predicts that the breakup time t for a perturbation wavelength $\lambda = (> \lambda_{min})$ relative to the minimum breakup time, t_{min}^{aniso}, associated with the kinetically favored wavelength, $\lambda = \lambda_{max}$, depends upon the ratio λ_{max}/λ as follows

$$\frac{t_{min}^{aniso}}{t} = \left(\frac{\lambda_{max}}{\lambda}\right)^2 \cdot \left(2 - \left(\frac{\lambda_{max}}{\lambda}\right)^2\right) \qquad (8)$$

The details of the anisotropy do not appear explicitly, and thus, the behavior from different channels with different values of λ_{max}, and from experiments conducted at different temperatures should in principle fall on one master curve. Fig. 4 shows the experimental results plotted in this manner. The values deduced for λ_{max} spanned roughly a factor of 2, while the minimum breakup times spanned a factor of ≈13. While the fit is not perfect, the results are reasonably well consolidated by this admittedly simple model. This suggests that there is some merit to this representation of the data, and that the approach used provides a valid starting point for dealing with the effect of anisotropy on such evolution processes.

In Rayleigh instabilities, the surface becomes increasingly perturbed as time increases, the range of surface orientations increases, and the driving force for mass flow also increases. When experimental results from such studies are interpreted using a model that incorporates a correction for surface energy anisotropy, the values of the apparent surface diffusion coefficient are somewhat higher than the average of values obtained in prior studies. In an ensuing section, we summarize observations from studies of pore shape changes, and show that when nonequilibrium shape pores are bounded by surfaces that are part of the Wulff shape, the evolution rates can be very low, and the inferred or apparent surface diffusion coefficients can be much lower than the average of values reported in prior studies. Thus, two experiments performed on the same material, but starting with different exposed surface orientations, and probing different portions of surface orientation space lead to considerably different estimates of the surface diffusivity. It emerges that in the case of pore shape equilibration, the mechanism of evolution may change from diffusion limited to SALK as the surface orientation is changed.

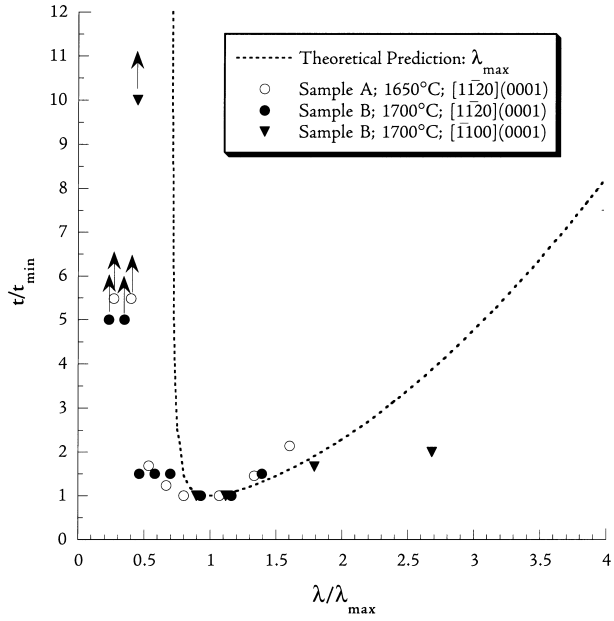

Fig 4. Plot of anneal time t required for breakup of pore channels with perturbation wavelength (pore spacing) λ. Anneal times are normalized by the minimum time for breakup, which corresponds to channels with wavelength λ equal to the kinetically favored wavelength λ_{max}. The data points at small values of λ/λ_{max} with upward arrows indicate that no breakup had occurred after the indicated normalized time. Samples A and B correspond to two samples with slightly different etch depths.

3.2 The energetics and kinetics of pore shape changes in alumina

Relative surface energies in a material can be determined through use of the Wulff theorem, eqn. (1). This requires that the equilibrium shape be reached, and that the relevant distances (Fig. 5), can be measured. The Herring scaling laws,[66] and predictions of evolution rates[67–69] suggest that for most materials, the equilibrium shape will be reached in reasonable times only if the particles or cavities undergoing shape changes are of micron size or smaller. Features in this size range are readily accessible using conventional microlithographic processing.

Experiments were performed using undoped sapphire (Crystal Systems, Salem, MA) of **m** (10$\bar{1}$0) orientation with a total cation impurity content of ≈70 ppm relative to Al. The wafers were cut to produce substrates 12·7×12·7×0·35 mm. A mask for photolithography was designed to produce three separate square arrays of pores with approximately square cross sections and pore dimensions of 2×2, 4×4 and 8×8 μm with 10 μm edge-to-edge spacing; each pore array had a size of 1×8 mm. The etch depth was ≈0·37 μm. The pores thus have a sufficiently fine size to reach equilibrium shapes in reasonable time periods. The ability to produce large numbers of nominally identical

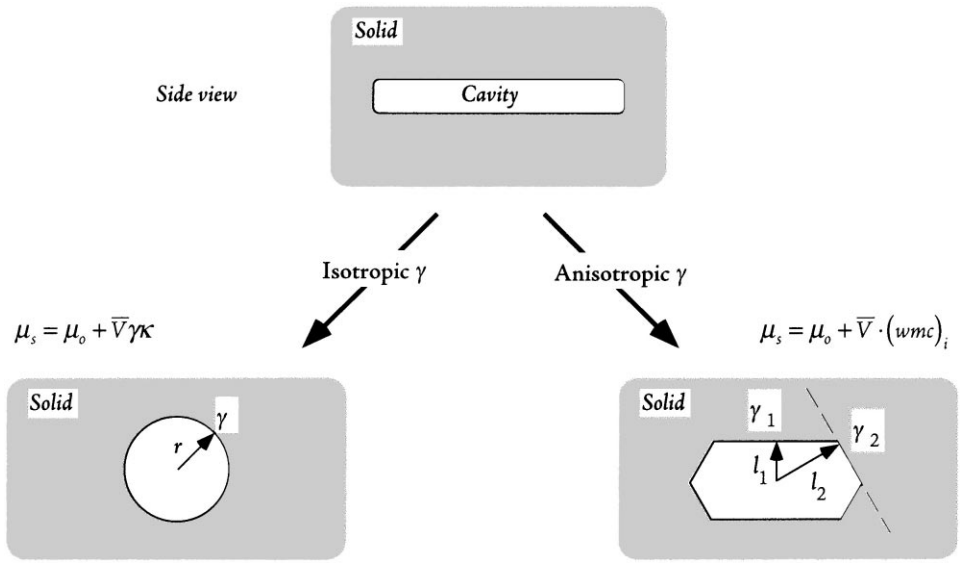

Fig. 5. Illustration of pore morphology changes in an isotropiac material (left) and in a material in which γ_i varies with orientation (right). In both cases, the equilibrium shape is reached when the chemical potential on the surface μ_s, is constant. For an isotropic material, this arises when the curvature κ is constant everywhere. For an anisotropic material, this arises when the weighted mean curvature (*wmc*) of each facet is the same. For the facetted crystal, when *wmc* is constant, the ratio γ_i/l_i is also constant. The result γ_i/l_i constant is basically the Wulff theorem.

pores allows measurements on many equilibrated pores, improving the statistical value of the data. Dense undoped polycrystals were produced from a high-purity alumina powder (Showa Denko, UA-5105), and determined to be equivalent in purity to the single crystals. A polished alumina polycrystal was placed onto the sapphire substrate, and they were bonded to one another by hot pressing in a graphite heating element hot press at 1300°C for 1 h in vacuum ($\approx 10^{-4}$ torr) with an applied pressure of 10 MPa. Once bonded, the pores are isolated from the furnace environment, avoiding the complications from contamination that can arise in experiments involving powder particles. By polishing the external surfaces of the bonded assemblies, the internal features can be examined using optical microscopy.

Anneals were performed in a W element furnace in flowing, gettered Ar at 1600°C for times up to 480 h and at 1800°C for times up to 80 h. During annealing, the single crystal consumes the polycrystal; the pore spacing and grain size were such that the pores separated from the single-crystal–polycrystal interface and were isolated within the single crystal. This eliminates the possibility that a grain boundary intersects the pore and modifies the observed shape. The morphological evolution of pores was monitored using optical microscopy. Once the coarsest pores had reached what appeared to be a time-independent shape, the sample was ground using a high-speed wheel with the plane containing the pores inclined slightly (1–2°) to the plane of polish. This exposed a strip of the pore array, while maintaining the other pores fully enclosed by sapphire. Grinding damage was removed by polishing. The pores exposed in this manner were examined using both a scanning electron microscope (SEM) and an atomic force microscope (AFM) to identify the facet structures. The information derived from one cross-section could then be used in a simulation to predict the pore structure as viewed from a different direction. Specimens providing views along different directions in the crystal were prepared to assure internal consistency in the observations. The evolution of equilibrium pore shapes in Ti^{3+}, Ti^{4+}, Ca^{2+}, and Mg^{2+} doped material was also examined using similar procedures, except that doped polycrystals were prepared. The interested reader is referred to Ref. 42 for a more detailed description of this work.

Figure 6(a) and (b) are SEM micrographs of exposed pores in undoped alumina annealed at 1600 and 1800°C, respectively. The sections shown expose surfaces parallel to the **m**-plane; samples were also cut to reveal sections parallel to the **a**-plane. A pore exposed parallel to the **m**-plane can supply data for **c** (0001) and $(11\bar{2}x)$-type planes. A pore exposed parallel to the **a**-plane can supply data for **c** (0001) and $(10\bar{1}x)$. Collectively, this set of data should provide complete information regarding the relative surface energies of low-index planes of alumina. The **c**- and **a**-facets can be easily identified from a knowledge of the orientation of the sapphire substrate. Other facets normal to the plane of the image are identified by the angles they make to the **c**-facet. For example, **r**-, **s**- and **p**-facets make angles of 57·6°, 72.4° and 61·2° to the **c**-facet, respectively. [The **p**-facets are of the $(11\bar{2}x)$ type.] Interfacet angles can be determined from AFM

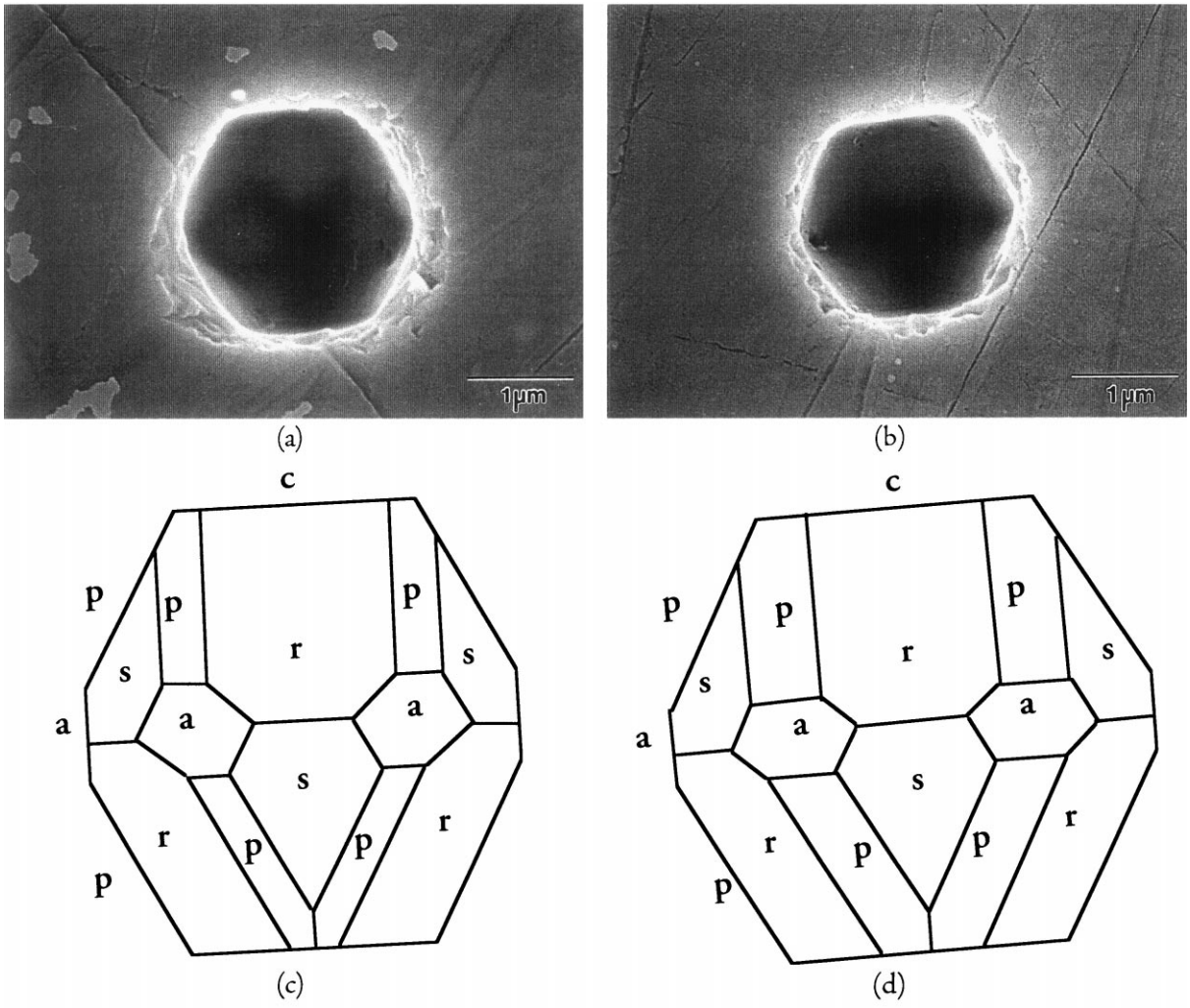

Fig. 6. SEM micrographs of pore morphology after annealing at (a) 1600°C and (b) 1800°C; the plane of polish is parallel to the **m**-plane. Equilibrium pore shapes at (c) 1600°C and (d) 1800°C when viewed along the same direction as in (a) and (b) as predicted from values of relative surface energies determined from cross sections of pores viewed along several different crystallographic directions.

traces taken along known crystallographic directions on surfaces of known orientation. Figure 6(c) and (d) are the simulated pore shapes corresponding to Fig. 6(a) and (b), respectively, with facets labelled. The relative surface energies, normalized by γ of the (0001) surface, that generate the simulated pore shapes consistent with the observations are summarized in Table 2, and compared with the values reported in the work of Choi *et al.*[69]

Several key features merit emphasis. The results agree with those of Choi et al. in the sense that the same five planes are identified as components of the Wulff shape of undoped alumina, the **c**-, **s**-, **r**-, **a**-, and **p**-planes; the **m**-plane, predicted to appear, is absent in this and all other doped specimens examined.[42] To our knowledge, the energy of the **p**-plane has not been calculated. At fixed temperature, the variation in the energy of stable surfaces is quite small, of the order of $\pm 10\%$ of the mean value. The results show that the relative energies change with temperature. In a pure system, one might expect the surface energy to decrease with increasing temperature due to entropy effects. In undoped systems, the degree of segregation will vary temperature, and this will add a second term to the temperature dependence of γ. It should also be noted that as a result of these two factors, the temperature dependencies of γ for different facets can be quite different, and thus affect the temperature dependence of the Wulff shape. We note that the values of the relative energies obtained in the present work do not agree with those reported by Choi *et al.* In the current study, the **r**-plane is found to have the lowest energy at both temperatures examined. It is possible that this reflects differences in the background impurity content of the two 'undoped' materials examined. The influence of background impurities and the effect of temperature may also contribute to the disparity that exists between computed and observed (Table 2) trends in the relative values of surface energy for low-index planes in alumina.

The extension of this method to studies of doped aluminas has revealed two broad categories of

Table 2. Experimentally determined relative surface energies of α-alumina

Plane	*1600°C; Choi* et al.[69]	*1600°C (this study)*	*1800°C (this study)*
c (0001)	1·0	1·0	1·0
s ($10\bar{1}1$)	1·07 ± 0·02	0·947 ± 0·016	1·042 ± 0·019
r ($10\bar{1}2$)	1·05 ± 0·02	0·855 ± 0·017	0·950 ± 0·0·030
a ($11\bar{2}0$)	1·22 ± 0·05	0·947 ± 0·026	1·080 ± 0·017
p ($11\bar{2}3$)	1·06 ± 0·02	0·957 ± 0·026	1·029 ± 0·016
m ($10\bar{1}0$)	> 1·16	> 1·008	> 1·115

behavior. In 500 ppm Ti^{3+} and 250 ppm Mg^{2+} doped materials, the effect of the dopant was to modify the relative surface energies, and to reduce the spread in relative values. One expects that this coincides with a reduced spread in the absolute values of the surface energies as well. The 'homogenizing effect' of Mg^{2+} is evident. In contrast to these dopants, Ti^{4+} and Ca^{2+} additions cause more major changes in the Wulff shape. In (500 ppm) Ti^{4+} doped material, the **s**- and **a**-planes are absent, and the equilibrium shape is a combination of **c**-, **r**-, and **p**-planes. In Ca^{2+}-doped material, a new **r**-type plane appears. The details of this work are the subject of several forthcoming publications.

The same experimental approach, but applied to larger pores that are initially farther from their equilibrium shape can be used to examine the kinetics of pore shape evolution, and to assess the effects of crystallography on the evolution process. By comparing the observations to the predictions of a model for surface-diffusion-controlled evolution, it is possible to infer whether the process is rate-limited by diffusion or instead controlled by surface-attachment/detachment processes or nucleation at the surface.[21,25,69,70]

The modelling of shape changes in facetted crystals due to surface diffusion has been the subject of several recent publications,[25,42,69,71] and is the focus of several forthcoming papers (e.g. Ref. 71) The key elements of the modelling are summarized here.

When a facetted crystal or a facetted cavity has the equilibrium shape, the weighted mean curvature (*wmc*),[72] and the chemical potential will be constant, and there is no driving force for mass transfer and shape changes. In contrast, when the shape deviates from the Wulff shape, the *wmc*, and the chemical potential will all vary from facet to facet on the surface of the particle or pore. This spatial variation in the chemical potential creates a driving force for mass transfer that allows the system to approach the equilibrium shape, albeit asymptotically. For mass transport controlled by surface diffusion, the surface flux, J_s, can be related to the gradient in the chemical potential at the surface. When the difference between the local potentials and the standard potential μ_o is small, then Fick's first law of diffusion for the surface flux (in atoms/m^2 s) can be written as

$$J_s = -\frac{D_s}{\bar{V}kT}\cdot\frac{d\mu}{dx} \tag{9}$$

where D_s is the surface diffusion coefficient, $\bar{V}$ is the molar volume, k is Boltzmann's constant, and T is absolute temperature.

If initially the chemical potential on the facet of a nonequilibrium shape crystal were constant on the entire facet, then discontinuities in the chemical potential would exist at the facet edges. These discontinuities would be rapidly eliminated, and after some transient, the chemical potential would be expected to vary with position on the facet such that the potential is continuous across the facet edge. In this paper, we specifically consider cases where the facets undergo uniform normal displacements. This requires that the rate of mass deposition or removal be uniform on each facet. The gradient or divergence of the flux must be constant on each facet, and this implies that $\nabla^2\mu$ be constant on each facet. The potential, and the gradient in the potential must be continuous at the facet edge.

If we have two facets, 1 and 2, that exchange mass, one approach to these diffusion problems is to determine the forms of $\mu_s^{(1)}$ and $\mu_s^{(2)}$ that satisfy the boundary conditions. Then, with a knowledge of the materials parameters, the mass addition/removal rates can be calculated. This is the essence of the method developed by Carter *et al.*, and presented in Refs 25 and 69. This approach is relatively simple to apply to 2-D problems, but satisfying the boundary conditions becomes very difficult when the diffusion problem is three-dimensional.

A simpler approach to dealing with 2-D problems, and more readily extended to 3-D cases, recognizes that regardless of the form of the chemical potential gradient on a facet, the total mass arrival rate for a facet is the sum of the mass flow rates at the facet edges. These flow rates are dictated by the gradients in the potential at the facet edges. If it is implicitly assumed that the deposition rate is uniform on the facet, the problem reduces to one of calculating or estimating the gradients at the facet

edges. Kitayama[42,71] approximates the gradient at the facet edge as the difference in the mean potentials on the adjoining facets divided by an 'average' diffusion distance, and considers a flux equation of the form

$$(J_s)_{2\to 1} = -\frac{D_s}{\overline{V}kT}\cdot\frac{\Delta\overline{\mu}_{2\to 1}}{\Delta x_{2\to 1}} \tag{10}$$

where $\Delta\bar{\mu}_{2\to1}=\bar{\mu}_1-\bar{\mu}_2$ represents the difference in mean potential, and $\Delta x_{2\to1}$ is the effective diffusion distance. The mean chemical potentials, $\bar{\mu}_1$ and $\bar{\mu}_2$ depend upon the weighted mean curvature. Recent work has shown that the two approaches to modelling give results that differ by only a factor of 1·5 for several different particle geometries.

The geometry of specific interest here is one in which we have a rectangular cross section in the x–y plane, and the pore or particle has infinite extent in the z-direction, as illustrated in Fig. 7. We consider a case in which the volume per unit depth is conserved, and for the 2-D case, this is equivalent to a condition of constant cross-sectional area, $A_{cs} = 4l_1l_2 =$ constant. Shape changes that conserve volume and involve normal displacements of the facets are thus subject to the constraint that

$$\mathrm{d}l_2 = -\frac{l_2}{l_1}\mathrm{d}l_1 \tag{11}$$

The driving force for the shape change is the reduction in total surface energy. This can be determined either by differential geometry, or by using the weighted mean curvature (*wmc*).[72] The differential surface energy change per unit depth of crystal due to a shape change will be given by

$$\begin{aligned}(\mathrm{d}F_s)_{\text{total}} &= (4\cdot1)\left[-\gamma_1\frac{l_2}{l_1}\mathrm{d}l_1 + \gamma_2\mathrm{d}l_1\right]\\ &= (4\cdot1)\left[\gamma_2 - \gamma_1\frac{l_2}{l_1}\right]\mathrm{d}l_1\end{aligned} \tag{12}$$

This expression equals zero when the Wulff condition, eqn (1), is satisfied. When l_2 exceeds the equilibrium value, the term in brackets is negative, and $\mathrm{d}F_s$ is negative when $\mathrm{d}l_1$ is positive.

If we consider the surface energy changes that arise when one transfers dn moles from a single surface of area A_2 per unit depth and energy γ_2 to a single surface of area A_1 per unit depth and energy γ_1, the appropriate expression for $\mathrm{d}F_s$ is

$$\begin{aligned}(\mathrm{d}F_s)_{2\to1} &= (2\cdot1)\left[-\gamma_1\frac{l_2}{l_1}\mathrm{d}l_1 + \gamma_2\mathrm{d}l_1\right]\\ &= (2\cdot1)\left[\gamma_2 - \gamma_1\frac{l_2}{l_1}\right]\mathrm{d}l_1\end{aligned} \tag{13}$$

The volume per unit depth swept due to the displacement of facet 1 by an amount $\mathrm{d}l_1$, $\mathrm{d}V_1$, can be related to the number of moles transferred dn and the molar volume, $\bar{V}$, as follows

$$\mathrm{d}V_1 \approx 2l_2\cdot1\cdot\mathrm{d}l_1 = \overline{V}\mathrm{d}n \;\Rightarrow\; \mathrm{d}l_1 = \frac{\overline{V}\mathrm{d}n}{2l_2\cdot1} \tag{14}$$

Inserting this into eqn (13) and rearranging, we obtain for the differential change of energy

$$(\mathrm{d}F_s)_{2\to1} = \overline{V}\left(\frac{\gamma_2}{l_2} - \frac{\gamma_1}{l_1}\right)\mathrm{d}n \tag{15}$$

The ratio of the free energy change and number of moles transferred is a chemical potential difference, and thus, we obtain

$$\begin{aligned}\left(\frac{\mathrm{d}F_s}{\mathrm{d}n}\right)_{2\to1} &= \Delta\mu_{2\to1} = \mu_1 - \mu_2\\ &= \overline{V}\left(\frac{\gamma_2}{l_2} - \frac{\gamma_1}{l_1}\right)\end{aligned} \tag{16}$$

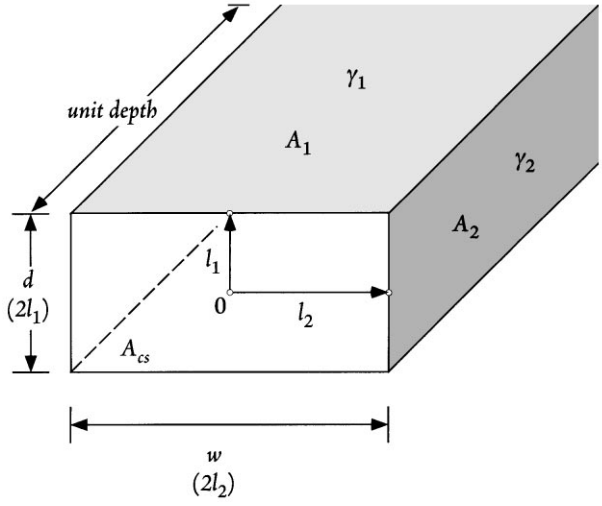

Fig. 7. Illustration of the stretched square geometry assumed in the modelling, and the parameters used in the geometric description.

The identical result can also be achieved if the difference in *wmc* of facets 1 and 2 is evaluated.[73]

The calculations of the displacement rates for facet 1 for the stretched square involves the following steps. The infinitesimal volume change of a single facet of type 1, dV_1, during an infinitesimal time interval dt is expressed as

$$dV_1 = A_1 dl_1 = J_s \cdot \delta_s \cdot L \cdot \Omega \cdot dt \tag{17}$$

where A_1 is the area per unit depth of facet 1, δ_s is the diffusion width or surface thickness, taken to be equal to $\Omega^{1/3}$ where Ω is the atomic volume, and L is the total common or shared edge length between the interacting facets. The product $\delta_s \cdot L$ represents the area through which diffusion is occurring. This equation can be rearranged and combined with eqn (10) to yield the following differential equation for the displacement rate of facet 1

$$\frac{dl_1}{dt} = \frac{J_s \cdot \delta_s \cdot L \cdot \Omega}{A_1} = -\frac{D_s \Omega^{4/3}}{\overline{V} kT} \cdot \frac{L}{A_1} \cdot \frac{\Delta \overline{\mu}_{2 \to 1}}{\Delta x_{2 \to 1}} \tag{18}$$

For the stretched square, with $\Delta \bar{\mu}_{2 \to 1}$ given by eqn. (16), $\Delta x_{2 \to 1}$ set equal to $(l_1 + l_2)/2$, and l_2 set equal to $A_{cs}/4l_1$, the potential gradient can be written as

$$\left(\frac{\Delta \mu}{\Delta x}\right)_{StrSq} = \frac{2\overline{V}\left(\frac{\gamma_2}{l_2} - \frac{\gamma_1}{l_1}\right)}{(l_1 + l_2)} = \frac{8\overline{V}}{A_{cs}}\left(\frac{\gamma_2 \cdot 4l_1^2 - \gamma \cdot A_{cs}}{4l_1^2 + A_{cs}}\right) \tag{19}$$

For unit depth of the stretched square, taking $A_1 = 2l_2 \cdot 1$, $L = 2$, and using eqn (19), eqn (18) takes the form

$$\left(\frac{dl_1}{dt}\right)_{StrSq} = -\frac{32 D_s \Omega^{4/3}}{kT} \cdot \frac{1}{A_{cs}^2} \cdot \frac{\gamma_2 \cdot 4l_3^1 - \gamma_1 \cdot l_1 A_{cs}}{4l_1^2 + A_{cs}} \tag{20}$$

Letting $R_{eq} = (\gamma_2/\gamma_1)$ this equation can be re-expressed as

$$\left(\frac{dl_1}{dt}\right)_{StrSq} = -\frac{32 D_s \Omega^{4/3} \gamma_1}{kT} \cdot \frac{1}{A_{cs}^2} \cdot \frac{l_1 (R_{eq} \cdot 4l_1^2 - A_{cs})}{4l_1^2 + A_{cs}} \tag{21}$$

Solving for dt and integrating leads to

$$(t - t_o)_{StrSq} = \left(\frac{kT}{D_s \Omega^{4/3} \gamma_1}\right)\left[\frac{A_{cs}^2}{32} \cdot \ln\left(\frac{l_1^{(t)}}{l_1^{(t_o)}}\right) - \frac{A_{cs}^2 (1 + R_{eq})}{64 R_{eq}} \cdot \ln\left(\frac{A_{cs} - 4(l_1^{(t)})^2 R_{eq}}{A_{cs} - 4(l_1^{(t_o)})^2 R_{eq}}\right)\right] \tag{22}$$

where $l_1^{(t_0)}$ is the value of l_1 at time t_0 and $l_1^{(t)}$ is the value of l_1 at time t. The predictions of this model can be compared with experimental results.

The experimental procedures employed to examine pore shape evolution were similar to those described for the Wulff shape experiments. Optical finish (premium grade) sapphire single crystal substrates with surface planes of the (0001), $\{10\bar{1}2\}$, $\{11\bar{2}0\}$ and $\{10\bar{1}0\}$ type (abbreviated as **c**, **r**, **a**, and **m**, respectively) were purchased from Meller Optics (Providence, RI). A mask containing a square array (250×250) of pores individually 16 × 16 μm with a 16 μm edge-to-edge spacing was fabricated, and 62500 identical surface cavities with a final size of ≈20 × 20 × 0.5 μm were lithographically introduced onto **c**, **r**, **a**, and **m** orientation sapphire substrates. A second (single crystal) substrate of identical orientation was placed upon the etched surface and aligned to produce, at worst, a very low angle misorientation ($\leqslant 1^\circ$) twist boundary. The two sapphire substrates were again bonded by vacuum hot pressing. The pore shapes after bonding and prior to annealing were essentially identical to those etched into the sapphire wafers [Fig. 8(a)]. Subsequent annealing was performed in a vacuum furnace at 1900°C. Samples were initially annealed for 4 h and then for an additional 12 h. Optical microscopy was used to follow the morphological evolution of the pores.

The sequence of Fig. 8(a)–(e) show the morphological evolution at 1900°C of internal pores in sapphire substrates of various surface orientations. Fig. 8(a) is indicative of the initial 'as-bonded' pore structure in *all* samples. Figure 8(b)–(e) show the shapes of pores etched into **c**, **r**, **a**, and **m**-oriented substrates, respectively, after total anneal times of 4 and 16 h at 1900°C. The substrate orientation, and thus, the crystallography of the surface that dominates the initial pore shape has a profound effect on the rate and nature of the morphological evolution. The **m**-orientation specimen evolved most rapidly and homogeneously. The **c**-orientation substrate exhibited the least shape change after 16 h at 1900°C. The **r**- and **a**-orientation specimens showed intermediate rates of evolution, and evolved inhomogeneously, some pores approaching the evolution rate characteristic of

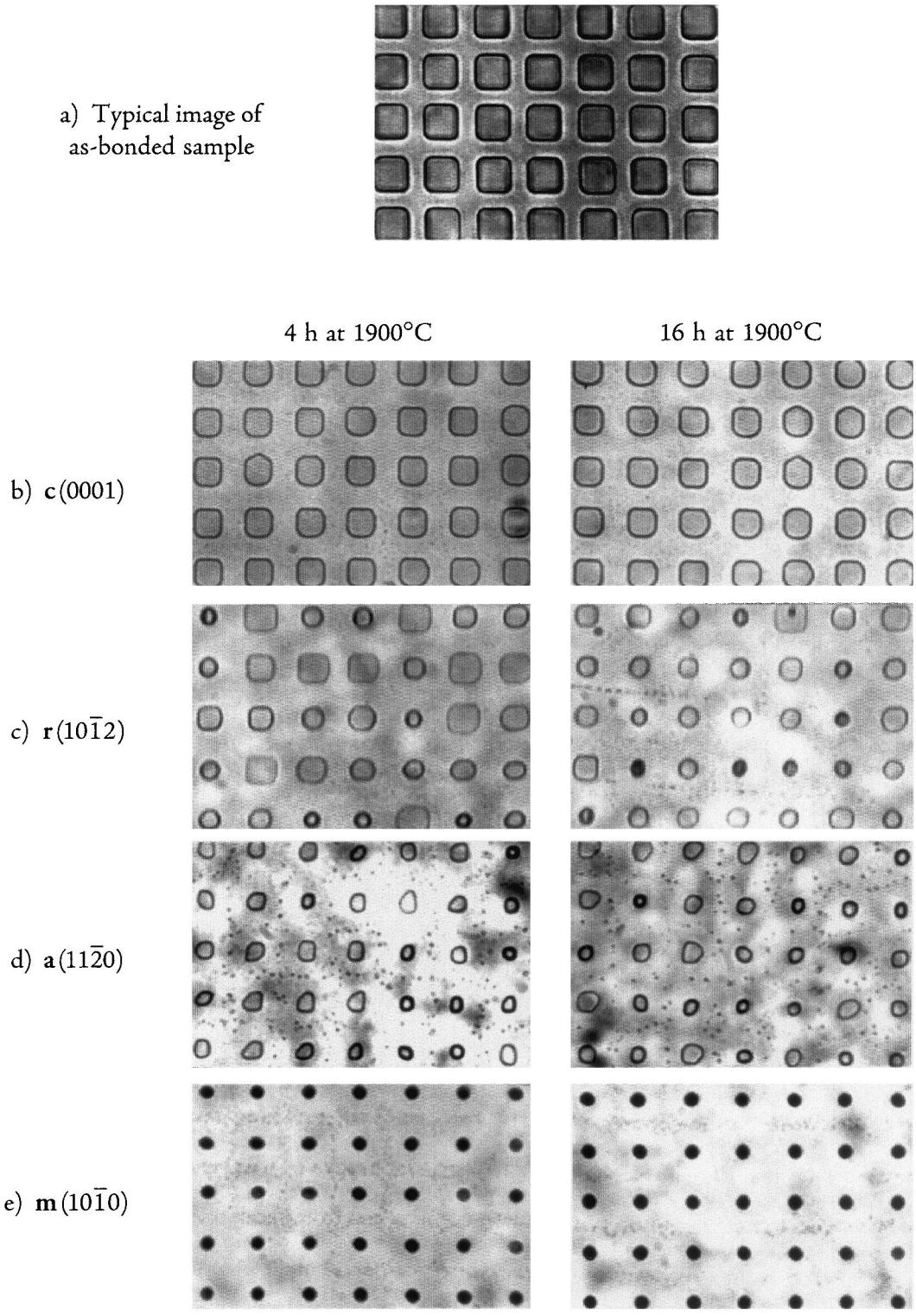

Fig. 8. Optical micrographs of internal pores in sapphire of varying surface orientation (a) after bonding, and (b)–(e) after anneals of 0, 4, and 16 h at 1900°C.

the **m**-orientation specimen extreme, and others exhibiting markedly smaller shape changes.

The predictions of a model based on surface diffusion control, eqn (22), and experimental measurements (≈20 representative pores in each sample for each annealing condition were examined) are compared in Fig 9. The error bars indicate the standard deviation in the measurement. In view of the results of the Wulff shape determinations, and the relatively modest effect of significantly larger variations in R_{eq} on the kinetics of evolution,[73] R_{eq} was set equal to one, and $\gamma_1 \approx \gamma_2 = 1{\cdot}0$ (J m^{-2}) was assumed. As mentioned previously, reported values of the $\delta_s D_s$ product for alumina vary by several orders of magnitude at fixed temperature. To reflect this in the calculations, values of $\delta_s D_s$ corresponding to the highest, (extrapolated) 'average' and lowest values for nominally pure materials,[54] $1{\cdot}23 \times 10^{-7}$, $1{\cdot}60 \times 10^{-9}$ and $2{\cdot}92 \times 10^{-10}$ (m^2 s^{-1}), respectively, at

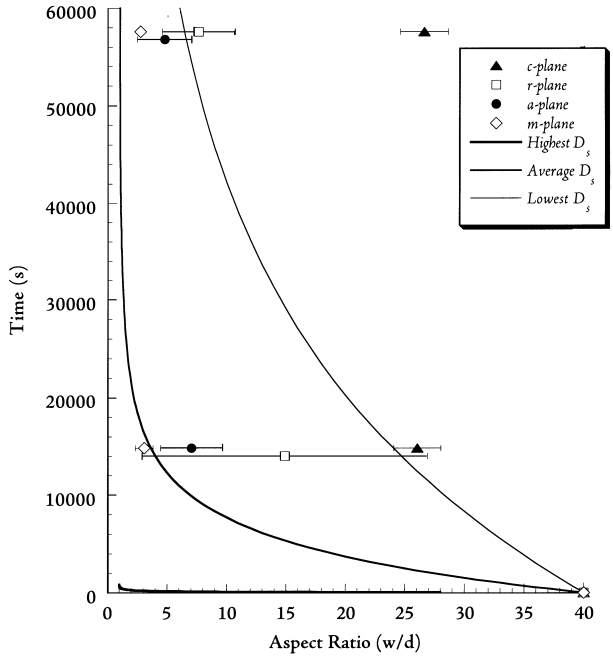

Fig. 9. Plot of computed times to reach specific w/d ratios at 1900°C as a function of $\delta_s D_s$, and comparison with experimental data (selected data points are shifted slightly on the time axis to allow better resolution of the error bars, all data are at 4 and 16h).

1900°C, and effective molecular volume, $\Omega = 2.11 \times 10^{-29}$ (m^3), were used as input parameters for the simulations.

There are several important features. It is clear that an interpretation of the results in terms of surface-diffusion-controlled evolution would require that $\delta_s D_s$ vary substantially with surface orientation, and also with time since the observed time-dependence of the w/d ratios crosses the lines or trajectories for fixed values of the diffusivity. Insistence on a surface diffusion interpretation requires a diffusivity that decreases with time (driving force). The Wulff shape experiments show that a roughly equiaxed pore should form. However, the observations of this study indicate that pores of distinctly nonequilibrium shape undergo relatively little shape change in the time interval from 4 to 16 h at 1900°C. This could be interpreted as indicating that the shape changes are diffusion-controlled only during the very early stages of evolution (possibly for anneals <4 h for some orientations), and that SALK-dominated behavior controls the later stages of evolution. Thus, it is only for the **m**-plane that the experiments are in good agreement with a surface diffusion model, and ironically, this is precisely the orientation for which the geometric assumptions in the model are most flawed. For the other three orientations, values of $\delta_s D_s$ that vary from being modestly lower than average to substantially lower than the lowest reported value of $\delta_s D_s$ are inferred.

The observed behavior suggests that the stability of the surface that dominates the as-bonded pore shape has an important influence on the evolution behavior. The results of Choi *et al.*[69] at 1600°C and the work of Kitayama[42] at 1600 and 1800°C have shown that the **c**(0001), **r**$\{10\bar{1}2\}$ and **a**$\{11\bar{2}0\}$ planes are components of the Wulff shape of undoped sapphire, whereas the **m**$\{10\bar{1}0\}$ plane is not. If we presume this to also be true at 1900°C, then the dominant bounding surfaces of cavities etched into **c**-, **r**-, and **a**-orientation substrates will be stable. Mass flow will cause the decay of local perturbations or irregularities in these stable surfaces. In general, the crystals are not perfectly oriented, and the large pore surfaces will develop ledges that are due to the miscut. As the pore shape evolves, these irregularities and miscut-related ledges that provide sources and sinks for adatoms during the initial stages of evolution, will tend to be removed. In the absence of a continuous supply of ledges, as might be provided by a screw dislocation, mass transfer may change from diffusion-limited to surface-attachment-limited. We speculate that the inhomogeneous evolution pattern of pores in the **r**- and **a**-orientation samples may reflect pores that do and do not intersect a dislocation that can generate surface defects, respectively. Similar conclusions relating to pore migration kinetics were reached in the work of Lemaire and Bowen.[74] The observations for the **c**-plane samples suggest that very few dislocations with Burgers vectors perpendicular to or inclined to the **c**-direction are present or intersect the surface.

In contrast, pore shape evolution in **m**-oriented substrates was rapid and uniform. The apparent $\delta_s D_s$ during the early stages of evolution is near the average value at this temperature, and then decreases slightly with increasing anneal time. The results of Choi *et al.*[69] and Kitayama[42] demonstrate that the **m**$\{10\bar{1}0\}$ plane is not part of the Wulff shape of undoped sapphire between 1600 and 1800°C. Rapid and spontaneous decomposition of the **m**-plane of undoped sapphire into a fine spatial scale hill-and-valley structure comprised of other low index planes at 1400°C has also been observed by Heffelfinger and Carter.[75] Similar changes at 1900°C would lead to structural disruption of the dominant bounding plane. Although the macroscopic orientation of the surface is maintained, microscopically the surface is rough. It is possible that the valleys formed at the intersection of two facets serve as a favorable site for nucleation of ledges, and that the ultimate decrease in the evolution rate may in part be due to the coarsening and ultimate disappearance of this hill-and-valley structure as the pore approaches its equilibrium shape.

4 Summary and Conclusions

Microdesigned interfacial defect structures have been shown to provide a vehicle for examining both the energetics of surfaces in alumina, and also for examining the kinetics of microstructural evolution. Experiments probing the Wulff shape of alumina indicate that the anisotropy of the surface energy is relatively small, a function of temperature, and influenced by impurity additions. However, experiments show that the spatial characteristics of evolution, or the temporal characteristics of evolution, or both are *strongly* affected by surface energy anisotropy. The root cause may be energetic, as in Rayleigh instabilities, or mechanistic, as appears to be the case in the studies of pore morphology changes. Vastly different *apparent* diffusivities can be deduced if surface energy anisotropy and the possibility of changes in rate-controlling mechanism are not considered. It is hoped that further experiments of the type described may be useful in probing the transition from diffusion-controlled to surface-attachment-limited kinetics, and thereby improving our understanding of microstructural evolution in ceramics.

Acknowledgements

The research described in this paper was primarily supported by the National Science Foundation under Grant No. DMR-9222644. The research dealing with an experimental determination of the Wulff shape of sapphire was supported by the National Science Foundation through a series of research grants (DMR-9222644, DMR-9617392). The work focussing on the kinetics of pore shape evolution and work by J. Rödel was supported by the Director, the Office of Energy Research, Office of Basic Energy Sciences, Materials Sciences Division of the US Department of Energy under Contract No. DE-AC03-76SF00098. We also acknowledge an NSF Equipment Grant No. DMR-9119460 which allowed the acquisition of hot pressing equipment critical to this work. Throughout the period of research we have benefitted from many helpful discussions with our colleagues. We are particularly grateful for many stimulating conversations with Rowland Cannon Jr. Finally, this work would not have been possible without the kind and continuing assistance of the staff of the Microfabrication Laboratory at the University of California.

References

1. Yan, M. F., Microstructural control in the processing of electronic ceramics. *Mater. Sci. Eng*, 1981, **48**(1), 53–72.
2. Brook, R. J., Fabrication principles for the production of ceramics with superior mechanical properties. *Proc. Brit. Ceram. Soc*, 1982, **32**, 7–24.
3. Shaw, N. J. and Brook, R. J., Structure and grain coarsening during the sintering of alumina. *J. Am. Ceram. Soc*, 1986, **69**(2), 107–110.
4. Quadir, T. and Readey, D. W., Microstructure development of zinc oxide in hydrogen. *J. Am. Ceram. Soc*, 1989, **72**(2), 297–302.
5. Kuczynski, G. C., Self-diffusion in sintering of metallic particles. *Trans. A.I.M.E*, 1949, **185**(2), 169–178.
6. Kingery, W. D. and Berg, M., Study of the initial stages of sintering of solids by viscous flow, evaporation–condensation, and self-diffusion. *J. Appl. Phys*, 1955, **26**(10), 1205–1212.
7. Coble, R. L., Sintering crystalline solids. I. Intermediate and final stage diffusion models. *J. Appl. Phys*, 1961, **32**(5), 787–792.
8. Nichols, F. A. and Mullins, W. W., Surface (interface) and volume-diffusion contributions to morphological changes driven by capillarity. *Trans. A.I.M.E*, 1965, **233**(10), 1840–1848.
9. Mullins, W. W., Flattening of a nearly plane solid surface due to capillarity. *J. Appl. Phys*, 1959, **30**(1), 77–83.
10. Mullins, W. W., Theory of thermal grooving. *J. Appl. Phys*, 1957, **28**(3), 333–339.
11. Sekerka, R. F. and Marinis, T. F., Dynamics of morphological change during solid-solid transformations. In *Solid→Solid Phase Transformations*, ed. H. I. Aaronson, D. E. Laughlin, R. F. Sekerka and C. M. Wayman. The Metallurgical Society of AIME, New York, 1982, pp. 67–84.
12. Robertson, W. M., Grain-boundary grooving by surface diffusion for finite surface slopes. *J. Appl. Phys*, 1971, **42**(1), 463–467.
13. Coblenz, W. S., Dynys, J. M., Cannon Jr., R. M. and Coble, R. L., Initial stage solid-state sintering models: a critical analysis and assessment. In *Sintering Processes*, ed. G. C. Kuczynski. Plenum Press, NY, 1980, pp. 141–157.
14. Choy, J. H., Hackney, S. A. and Lee, J. K., Nonlinear stability analysis of the diffusional spheroidization of rods. *J. Appl. Phys*, 1995, **77**(11), 5647–5654.
15. Wulff, G., Zur Frage der Geschwindigkeit des Wachstums und der Auflösung der Krystallflachen. *Z. Krist*, 1901, **34**, 449–530.
16. Brailsford, A. D. and Gjostein, N. A., Influence of surface energy anisotropy on morphological changes occurring by surface diffusion. *J. Appl. Phys*, 1975, **46**(6), 2390–2397.
17. Bonzel, H. P., Preuss, E. and Steffen, B., Periodic surface profiles under the influence of anisotropic surface energy: a steady-state solution. *Surface Science*, 1984, **145**(1), 20–32.
18. Bonzel, H. P., Preuss, E. and Steffen, B., The dynamical behavior of periodic surface profiles on metals under the influence of anisotropic surface energy. *J. Appl. Phys. A (Solids and Surfaces)*, 1984, **35**(1), 1–8.
19. Breuer, U. and Bonzel, H. P., Morphology of periodic surface profiles on Au single crystals and the anisotropy of the surface free energy of Au. *Surface Science*, 1992, **273**(1), 219–236.
20. Surnev, S., Voigtländer, B., Bonzel, H. P. and Mullins, W. W., Anisotropic profile decay on perturbed Au(111) vicinal surfaces. *Surface Science*, 1996, **360**(1), 242–248.
21. Bonzel, H. P. and Mullins, W. W., Smoothing of perturbed vicinal surfaces. *Surface Science*, 1996, **350**(1), 285–300.
22. Duport, C., Chame, A., Mullins, W. W. and Villain, J., Decay of grooves cut in a surface with singular orientation when the neighboring orientations are unstable. *J. Phys. I France*, 1996, **6**, 1095–1125.
23. Taylor, J. E., Overview No. 98 II — mean curvature and weighted mean curvature. *Acta Metall. Mater*, 1992, **40**(7), 1475–1485.
24. Cahn, J. W. and Taylor, J. E., Surface motion by surface diffusion. *Acta Metall. Mater*, 1994, **42**(4), 1045–1063.

25. Carter, W. C., Roosen, A. R., Cahn, J. W. and Taylor, J. E., Shape evolution by surface diffusion and surface attachment limited kinetics on completely facetted surfaces. *Acta Metall. Mater*, 19995, **43**(12), 4309–4323.
26. Rödel, J. and Glaeser, A. M., Production of controlled morphology intergranular pore arrays: implications and opportunities. *J. Am. Ceram. Soc*, 1987, **70**(8), 172–175.
27. Rödel, J. and Glaeser, A. M., Microdesigned interfaces: new opportunities for materials science. *Yogyo Kyokai Shi*, 1991, **99**(4), 251–265.
28. Rödel, J. and Glaeser, A. M., High-temperature healing of lithographically introduced cracks in sapphire. *J. Am. Ceram. Soc*, 1990, **73**(3), 592–601.
29. Powers, J. D. and Glaeser, A. M., High-temperature healing of cracklike flaws in Mg- and Ca-Ion-implanted sapphire. *J. Am. Ceram. Soc*, 1992, **75**(9), 2547–2558.
30. Powers, J. D. and Glaeser, A. M., High-temperature healing of cracklike flaws in titanium ion-implanted sapphire. *J. Am. Ceram. Soc*, 1993, **76**(9), 2225–2234.
31. Kulinsky, L., Powers, J. D. and Glaeser, A. M., Morphological evolution of pre-perturbed pore channels in sapphire. *Acta Mater*, 1996, **44**(10), 4115–4130.
32. Rödel, J. and Glaeser, A. M., Pore drag and pore-boundary separation in alumina. *J. Am. Ceram. Soc*, 1990, **73**(11), 3302–3312.
33. Rödel, J. and Glaeser, A. M., Anisotropy of grain growth in alumina. *J. Am. Ceram. Soc*, 1990, **73**(11), 3292–3301.
34. Powers, J. D. and Glaeser, A. M., Titanium effects on sintering and grain boundary mobility of alumina. *Ceram. Eng. Sci. Proc*, 1997, **18**(4), 617–623.
35. Rödel, J. and Glaeser, A. M., A technique for investigating the elimination and coarsening of model pore arrays. *Mater. Lett*, 1988, **6**(10), 351–355.
36. Tasker, P. W., Surfaces of magnesia and alumina. In *Advances in Ceramics*, Vol. 10, ed. W. D. Kingery. The American Ceramic Society, Columbus, OH, 1984, pp. 176–189.
37. Hartman, P., The effect of surface relaxation on crystal habit: cases of corundum (α-Al_2O_3) and hematite (α-Fe_2O_3). *J. Crystal Growth*, 1989, **96**, 667–672.
38. Mackrodt, W. C. and Tasker, P. W., Segregation isotherms at the surfaces of oxides. *J. Am. Ceram. Soc*, 1989, **72**(9), 1576–1583.
39. Davies, M. J., Kenway, P. R., Lawrence, P. J., Parker, S. C., Mackrodt, W. C. and Tasker, P. W., Impurity segregation to the surfaces of corundum-structured oxides. *J. Chem. Soc. Faraday Trans 2*, 1989, **85**(5), 555–563.
40. Manassidis, I. and Gillan, M. J., Structure and properties of alumina surfaces calculated from first principles. *J. Am. Ceram. Soc*, 1994, **77**(2), 335–338.
41. Gilmore, R. S., Glaeser, A. M. and Wade, J. C., Calibrating ultrasonic images for the NDE of structural materials. *Trans. ASME (Journal of Engineering for Gas Turbines and Power)*, 1994, **116**(3), 640–646.
42. Kitayama, M., The Wulff shape of doped and undoped sapphire. Ph.D. thesis, Department of Materials Science and Mineral Engineering, University of California, Berkeley, December 1996.
43. Kitayama, M. and Glaeser, A. M., A new method for determining the Wulff shape of alumina. In *Sintering Technology*, ed. R. M. German, G. Messing and R. G. Cornwall. Chapman-Hall, London, 1996, pp. 285–292.
44. Roberts, W. M. and Eckstrom, F. E., Impurity effects in surface diffusion on aluminum oxide. *Mater. Sci. Res*, 1969, **4**, 273–283.
45. Prochazka, S. and Coble, R. L., Surface diffusion in the initial sintering of alumina: I. *Phys. Sintering*, 1970, **2**(1), 1–18.
46. Prochazka, S. and Coble, R. L., Surface diffusion in the initial sintering of alumina: II. *Phys. Sintering*, 1970, **2**(2), 1–14.
47. Prochazka, S. and Coble, R. L., Surface diffusion in the initial sintering of alumina: III. *Phys. Sintering*, 1970, **2**(2), 15–34.
48. Rao, W. R. and Cutler, I. B., Initial sintering and surface diffusion in Al_2O_3. *J. Am. Ceram. Soc*, 1972, **55**(3), 170–171.
49. Achutaramaya, G., Ph.D. thesis, University of Washington, 1972 (cited in Ref. 57).
50. Yen, C. F. and Coble, R. L., Spheroidization of tubular voids in Al_2O_3 crystals at high temperature. *J. Am. Ceram. Soc*, 1972, **55**(10), 507–509.
51. Moriyoshi, Y. and Komatsu, W., Kinetics of initial combined sintering. *Yogyo Kyokai Shi*, 1973, **81**(3), 102–107.
52. Huang, F. H., Henrichson, R. A. and Li, C. Y., A study of capillarity and mass transport on the Al_2O_3 Surface. *Mater. Sci. Res*, 1975, **10**, 173–186.
53. Maruyama, T. and Komatsu, W., Surface diffusion of single-crystal Al_2O_3 by scratch-smoothing method. *J. Am. Ceram. Soc*, 1975, **58**(7-8), 338–339.
54. Gupta, T. K., Instability of cylindrical voids in alumina. *J. Am. Ceram. Soc*, 1978, **61**(5-6), 191–195.
55. Kitazawa, K., Komaki, I., Matsukawa, K. and Fueki, K., Surface Mass transport study of alumina and magnesium aluminum spinel by multiple scratch smoothing. *Yogyo Kyokai Shi*, 1980, **88**(2), 92–99.
56. Monty, C. and LeDigou, J., Effect of MgO on surface diffusion in alumina. *High Temp. — High Pressures*, 1982, **14**, 709–716.
57. Bennison, S. J. and Harmer, M. P., Effect of magnesia solute on surface diffusion in sapphire and role of magnesia in the sintering of alumina. *J. Am. Ceram. Soc*, 1990, **73**(4), 833–837.
58. Asoga, A. and Nikopoulous, P., Groove angles and surface mass transport in polycrystalline alumina. *J. Am. Ceram. Soc*, 1994, **77**(4), 954–960.
59. Stölken, J. S. and Glaeser, A. M., The morphological evolution of cylindrical rods with anisotropic surface free energy via surface diffusion. *Scripta Metall. et Mater*, 1992, **27**(4), 449–454.
60. Glaeser, A. M., A new approach to investigating surface transport in ceramics. In *Mass and Charge Transport in Ceramics, Ceramic Transactions*, Vol. 71, ed. K. Koumoto, L. M. Sheppard and H. Matsubara. American Ceramic Society, Colubus, OH, 1996, pp. 117–136.
61. Glaeser, A. M., Investigating surface transport in ceramics using microdesigned interfaces. In *Ceramic Interfaces: Properties and Applications*, ed. R. St. Smart. The Institute of Materials, London, 1998, pp. 241–282.
62. Plateau, M. T., On the recent theories of the constitution of jets of liquid issuing from circular orifices. *Phil. Mag. S4*, 1865, **12**(79), 286–297.
63. Lord Rayleigh, On the instability of jets. *Proc. London Math. Soc*, 1879, **10**, 4–13.
64. Nichols, F. A. and Mullins, W. W., Morphological changes of a surface of revolution due to capillarity-induced surface diffusion. *J. Appl. Phys*, 1965, **36**(6), 1826–1835.
65. Cahn, J. W., Stability of rods with anisotropic surface free energy. *Scripta Metall*, 1979, **13**(11), 1069–1071.
66. Herring, C., Effect of change of scale on sintering phenomena. *J. Appl. Phys*, 1950, **21**(4), 301–303.
67. Kern, R., The equilibrium form of a crystal. In *Morphology of Crystals, Part A: Fundamentals*, ed. I. Sunagawa. Terra Scientific, Tokyo, 1987, pp. 92–98.
68. Nelson, R. S., Mazey, D. J. and Barnes, R. S., The thermal equilibrium shape and size of holes in solids. *Phil. Mag*, 1965, **11**, 91–111.
69. Choi, J., Kim, D., Hockey, B. J., Wiederhorn, S. M., Handwerker, C. A., Blendell, J. E., Carter, W. C. and Roosen, A. R., The equilibrium shape of internal cavities in sapphire. *J. Am. Ceram. Soc*, 1997, **80**(1), 62–68.
70. Searcy, A. W. and Bullard, J. W., Thermodynamics and kinetics of surface area changes of faceted particles. *J. Am. Ceram. Soc*, 1994, **77**(9), 2314–2318.
71. Kitayama, M. and Glaeser, A. M., The kinetics of pore shape evolution in alumina. *J. Mater. Synth. Proc.*, 1998, **6**(13), 161–167.
72. Taylor, J. E., Overview no. 98 II — mean curvature and weighted mean curvature. *Acta Metall. Mater*, 1992, **40**(7), 1475–1485.

73. Kitayama, M., Narushima, T., Carter, W. C., Cannon, R. M. Jr, and Glaeser, A. M., The Wulff shape of alumina: I. Modelling the kinetics of morphological evolution, in preparation.
74. Lemaire, P. J. and Bowen, H. K., Migration of small pores in potassium chloride due to a temperature gradient. *J. Am. Ceram. Soc*, 1982, **65**(1), 49–52.
75. Heffelfinger, J. R. and Carter, C. B., Faceting of ceramic surfaces. *J. Am. Ceram. Soc*., 1996, **79**(11), back cover.